Combined experimental and theoretical probe of the branching fractions of the $4P_{3/2}$ state in $^{40}Ca^+$

Hong-Fang Song,[1,3,4,5,6,*] Yong-Bo Tang,[2,*] Shao-Long Chen,[1,3,4,5] Li-Jun Du,[7] Yao Huang,[1,3] Hua Guan,[1,3,†] and Ke-Lin Gao[1,3,‡]

[1]*State Key Laboratory of Magnetic Resonance and Atomic and Molecular Physics, Wuhan Institute of Physics and Mathematics, Chinese Academy of Sciences, Wuhan 430071, People's Republic of China*

[2]*College of Engineering Physics, Shenzhen Technology University, Shenzhen, 518118, People's Republic of China*

[3]*Key Laboratory of Atomic Frequency Standards, Wuhan Institute of Physics and Mathematics, Chinese Academy of Sciences, Wuhan 430071, People's Republic of China*

[4]*Center for Cold Atom Physics, Chinese Academy of Sciences, Wuhan 430071, People's Republic of China*

[5]*University of Chinese Academy of Sciences, Beijing 100049, People's Republic of China*

[6]*School of Science, Huzhou Teachers College, Huzhou 313000, People's Republic of China*

[7]*China Academy of Space Technology, Xi'an 710100, People's Republic of China*

(Received 12 July 2019; revised manuscript received 8 October 2019; published 14 November 2019)

In this work, we carry out experimental measurements and theoretical calculations of the branching fractions for the $4P_{3/2}$ state of $^{40}Ca^+$. The measurements are based on counting photon numbers emitted from hundreds of ions trapped in a linear Paul trap, as their being affected by lasers. The calculations are performed using the relativistic coupled-cluster method at different approximations. The measured values for the decays of the $4P_{3/2}$ state into the $4S_{1/2}$, $3D_{5/2}$, and $3D_{3/2}$ states are, respectively, 0.9350(4), 0.0587(4), and 0.0063(2), which agree well with our recommended theoretical values 0.9344(13), 0.0590(12), and 0.0066(1). Our measured values are also consistent with the experimental values of Gerritsma *et al.* [R. Gerritsma, G. Kirchmair, F. Zähringer, J. Benhelm, R. Blatt, and C. F. Roos, Eur. Phys. J. D **50**, 13 (2008)] using a completely different method. Furthermore, we also calculate the branching fractions of the $4P_{1/2}$ state using the same method, and compare to the available experimental and theoretical data.

DOI: 10.1103/PhysRevA.100.052505

I. INTRODUCTION

Accurate knowledge of atomic properties of the singly ionized calcium ion Ca^+ is of great importance for the development of ultraprecise atomic clocks [1,2] and quantum information [3,4], for testing the Lorentz invariance [5,6], and for investigating radiative properties of stellar objects [7,8]. There have been a number of theoretical studies of Ca^+ atomic structure properties [9–20], including energy levels, electromagnetic transition matrix elements, polarizabilities, hyperfine structure constants, lifetimes, and branching fractions. Some of the atomic properties have also been measured, such as the magic wavelengths [21], isotope shifts [22], polarizabilities [23,24], branching fractions [25–27], transition matrix elements [27,28], and lifetimes [29–35]. Among these properties, a significant difference between theory and experiment is observed for the branching fractions of the $4P_{1/2}$ state. Ramm *et al.* [26] accurately measured the branching fractions of the $4P_{1/2}$ state using a method based on time-resolved recording of atomic fluorescence during a series of population transfers. Hettrich *et al.* [27] determined the branching fraction of the $4P_{1/2}$ state by comparing dispersive and absorptive light-ion interactions. Though these two measurements agree with each, all theoretical results obtained using various atomic structure models are outside the uncertainties of the measured values. However, the agreement between these two measurements for the $4P_{1/2}$ state suggests that more precise theoretical calculations need to be carried out or atomic structure models need to be further optimized. For the branching fractions of the $4P_{3/2}$ state of Ca^+, on the other hand, there exists only one measurement by Gerritsma *et al.* [25] using a novel technique based on monitoring population transfer while repeatedly pumping the ions between different internal states. It is, therefore, desirable to have an independent verification of their results using an alternative method.

After the pioneering work of the sequential photon-counting method [26], several groups followed this method and accurately measured the branching ratios of other alkaline-earth metal ions [36–39]. Most of these applications are for $nP_{1/2}$ states because for the $nP_{3/2}$ state, the photon counting is sensitive to the laser polarization and magnetic field. Thus, the Hanle effect is an important source of uncertainty that needs to be considered carefully when the branching fractions of the $4P_{3/2}$ state are measured using this method. By setting the so-called "magic angle" [40] between the laser polarization and magnetic field, Zhang *et al.* [38] measured the branching fractions for both the $5P_{3/2}$ and $5P_{1/2}$ states of $^{88}Sr^+$ with high accuracy. However, calibration of the magic angle is difficult because one needs to know precisely

*These two authors contributed equally to this work.
†guanhua@wipm.ac.cn
‡klgao@wipm.ac.cn

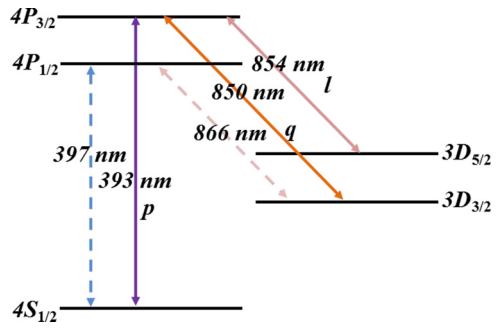

FIG. 1. Level scheme of $^{40}Ca^{+}$. The 393-nm laser is the cooling laser. Both the 850- and 854-nm lasers are used to repump the ions at the metastable states $3D_{3/2}$ and $3D_{5/2}$ back to $4P_{3/2}$ for continuous laser cooling. The branching fractions are measured for the decays of $4P_{3/2}$ into $4S_{1/2}$, $3D_{3/2}$, and $3D_{5/2}$, which are labeled as p, q, and l, respectively. The $4P_{1/2}$ state is only 4 nm in energy below $4P_{3/2}$, and the relevant lasers of 397 and 866 nm that may affect these decay processes are also depicted.

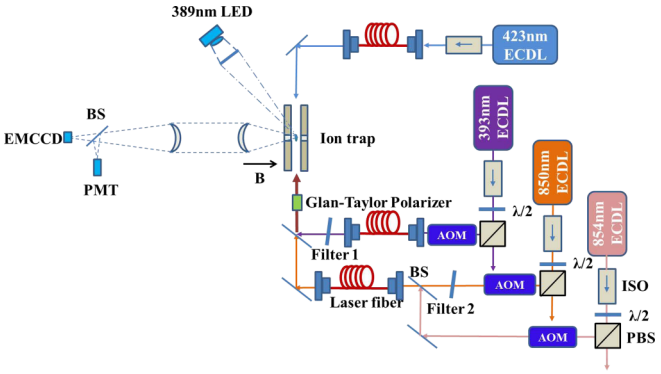

FIG. 2. Schematic diagram of the experimental setup. Between the trap and BS are several lens that zoom up the image of ions. After the light is passed through PBS, it is guided into the transfer cavities for laser frequency stabilization (not drawn). In the diagram, external-cavity diode laser (ECDL), $\lambda/2$: 1/2 wave plate, optical isolator (ISO), polarized beam splitter (PBS), acousto-optic modulator (AOM), beam splitter (BS), photoelectric multiplier tube (PMT), electron-multiplying camera (EMCCD).

the direction of the magnetic field, the direction of laser polarization, and the polarizer holder's scale. In this work, we will measure the branching fractions for the $4P_{3/2}$ state of $^{40}Ca^{+}$ by counting photons from hundreds of ions trapped in a linear Paul trap interacting with lasers. We will detect photons at different angle between the light polarization and magnetic field and establish a relationship between the branching fraction and the angle for uncertainty evaluation. Then the photon numbers will be recorded at two specific directions with an angle of 109.4°, and the mean value of these two results is the branching fraction. The advantage of this approach is that it does not require any calibration of the laser polarization direction. To support our measurement results, we will also calculate the branching fractions for the $4P_{1/2}$ and $4P_{3/2}$ states of Ca^{+} using the relativistic coupled-cluster method under four approximation schemes. The recommended values and uncertainties will be given and comparisons to the available experimental and theoretical data will be made.

The remaining part of this paper is organized as follows. Section II gives the details about the experimental method, setup, procedure, and data analysis. Theoretical results are presented in Sec. III, together with comparisons to other results. A summary is given in Sec. IV.

II. EXPERIMENTAL METHOD AND RESULTS

A. Experimental method, setup, and procedure

We first sketch the general principles of our measurements. A level scheme of $^{40}Ca^{+}$ is shown in Fig. 1, where the five lowest-lying states and the relevant electric dipole-allowed transitions are marked. The 393-nm laser pumps the ground-state ions to the $4P_{3/2}$ state, and then the ions scatter photons of 393, 850, and 854 nm with the fractions of p, q, and l, respectively. If we detect the 393-nm fluorescence for long-enough time, then the mean number of photons will be

$$\langle N_{393}\rangle = \frac{p}{1-p}\varepsilon_{393}, \tag{1}$$

where ε_{393} is the detection efficiency at 393 nm. Then, turning on both the 850- and 854-nm lasers for a long-enough period of time, the mean number of photons will be

$$\langle N_{850,854}\rangle = \varepsilon_{393}. \tag{2}$$

If only the 850-nm laser is turned on, we will detect the mean number of photons as

$$\langle N_{850}\rangle = \frac{pq}{(1-p)(1-q)}\varepsilon_{393}. \tag{3}$$

Similarly, turning on the 854-nm laser only will lead to the mean number of photons to be

$$\langle N_{854}\rangle = \frac{pl}{(1-p)(1-l)}\varepsilon_{393}. \tag{4}$$

According to the condition $p+q+l=1$, we can obtain p, q, and l as

$$\begin{cases} p = \frac{N_{393}}{N_{393}+N_{850,854}}, \\ q = \frac{N_{850}}{N_{393}+N_{850}}, \\ l = \frac{N_{854}}{N_{393}+N_{854}}. \end{cases} \tag{5}$$

We can see from above that once $\langle N_{393}\rangle$, $\langle N_{850,854}\rangle$, and $\langle N_{850}\rangle$ are detected, we can determine p and q directly, and determine l from $l = 1-p-q$.

The detailed description of the linear Paul trap used in our experiment may be found in Ref. [41]. $^{40}Ca^{+}$ ions were trapped with the radio frequency of 3.8 MHz and the amplitude of 210 V_{pp}. The voltage applied between two endcaps was 2.0 V. The schematic diagram of the whole setup is shown in Fig. 2. All lasers were introduced into the trap by polarization maintaining fibers. The 389-nm LED and the 423-nm laser were used to generate $^{40}Ca^{+}$. Both the cooling laser of 393 nm and the repumping lasers of 850 and 854 nm were stabilized with transfer cavities [42] and passed through the acoustooptic modulators (AOMs) before being coupled into fibers. The

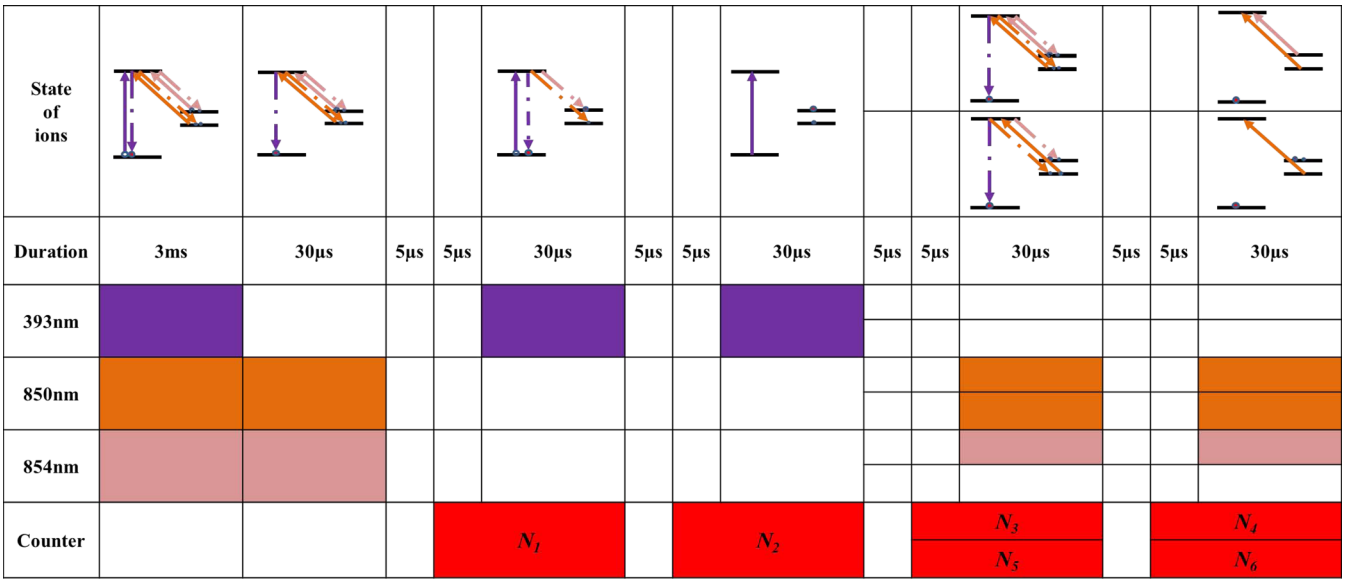

FIG. 3. Time sequence diagram and ion energy states at different stages of branching fraction measurement. To ensure that all ions are prepared in the ground state, the 850- and 854-nm lasers last for an extra duration of 30 μs. To avoid omission of photon counting, the photon counter is turned on before light's arrival. Because the photon counter has a dead time of 2 ms, we need to repeat the previous part of the sequence when we make second measurement. After detecting N_2, it is necessary to detect either N_3 or N_5; in other words, N_3 and N_5 are equivalent in measurement. So are N_4 and N_6. For simplicity, we put them in the same columns.

filters (Semrock, FF01-387/480 and FF01-832/37) labeled as "Filter 1" and "Filter 2" were applied along the light paths of 393- and 850-nm to filter out small amount of 397- and 854-nm lights produced by the laser diodes. A Glan-Taylor polarizer (Union Optic PGT 5010) was inserted before the light's striking on the vacuum chamber to change the laser polarization. A 2.5 G magnetic field was applied along the direction shown in Fig. 2. Both PMT (ET Enterprises, 9893/350B) and EMCCD (Andor, iXon885) monitored the fluorescence scattered by the ions in the direction perpendicular to the trap axis.

To obtain the branching fractions, we need to record the photon number at 393 nm at different moments. Our experimental steps are briefly sketched in Fig. 3. After a 3-ms cooling, the 854- and 850-nm lights lasted for another 30 μs to ensure that all the ions were in the ground state before the next step starts. The ions were shelved into the D states after being affected by the 393-nm laser for a sufficiently long period of time, which resulted in no fluorescence afterwards; however, since the 393-nm laser was still on, the second detection gave the number of photons coming from laser scattering noise only. The number of photons coming from the ions can be determined according to $\langle N_{393}\rangle = N_1 - N_2$, where N_1 is the number of photons detected in the process of the 393-nm light interaction after the cooling is finished, and N_2 is the number of background photons. Next, since the 850- and 854-nm lasers had been on for long-enough time, the ions were pumped back to the ground state emitting the 393-nm photons with N_3 counts. Since the ions in the ground state could not be affected by either the 850- or 854-nm laser, N_4 would represent the background counts. Replacing the 850- and 854-nm pulses with only the 850-nm pulse, we could obtain N_5 and N_6. The quantities $\langle N_{850,854}\rangle$ and $\langle N_{850}\rangle$ can be expressed as $N_3 - N_4$ and $N_5 - N_6$, respectively. A photon counter (Stanford Research Systems, SR400) used has the dwell time of 2 ms. During this period of time, counting was disabled. So in the diagram, we insert the steps of cooling (3 ms) and repumping (30 μs) followed by the necessary steps to keep the ions in certain states before detection.

The Glan-Taylor polarizer was placed in the light path to change laser's polarization. We rotated the prism from -60° to 70° (these angles are labeled and shown on the prism holder and they are not the true angles between the laser polarization and magnetic field) and measured the photon counting at every 10° for 40 000 cycles. At each angle, the measurement was repeated ten times and then averaged. The branching fraction was not changed when the angle between the light polarization and magnetic field was unchanged, causing the data symmetric about the angle of 5°. On each side, the branching fraction is linear with respect to the angle, as shown in Fig. 4. The true branching fractions are located at the angle of 54.7°. However, the direction of the magnetic field is difficult to determine precisely. One set of data was taken at the angle of 63° with 61 measurements, and then when the prism was rotated to -46.4°, another set of data was taken with 61 measurements. The average of the two data sets is equal to the one taken at the magic angle of 54.7°. At 63°, the measured branching fractions were 0.9340(7) for the $4P_{3/2} - 4S_{1/2}$ decay and 0.0065(2) for the $4P_{3/2} - 3D_{3/2}$ decay with only statistical errors included. At -46.4°, these branching fractions were measured to be 0.9360(5) and 0.0060(2), respectively.

B. Experimental results and data analysis

The main sources of error in measurement include counting statistics, finite laser durations, extinction ratio of AOMs,

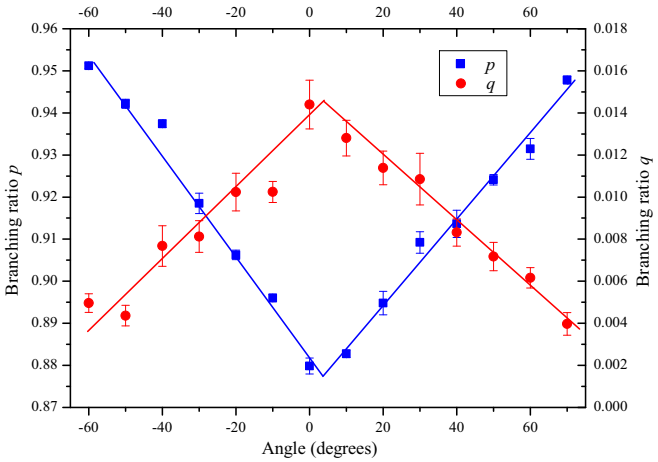

FIG. 4. Branching fractions at different angles shown on the dial of the prism fixer. The branching fractions p and q are, respectively, for $4P_{3/2} - 4S_{1/2}$ and $4P_{3/2} - 3D_{3/2}$. The branching fractions reach their extreme ones at the angle about 5°, that is to say, the laser polarization is in the direction of magnetic field when we rotate the prism to 5°. Each point is measured ten times.

finite lifetimes of D states, impure light from laser diodes, off-resonant excitation, polarization alignment of laser with respect to the magnetic field, and ions losing. All the uncertainties in the branching fractions for the $4P_{3/2} - 4S_{1/2}$ and $4P_{3/2} - 3D_{3/2}$ decays are listed in Tables I and II.

Our method for measuring the branching fractions is based on long-term interaction time between light and ions to make sure that all the ions are pumped to certain states. Since the ions are irradiated by lasers for only 30 μs during the detection period, we must have underestimated photon scattering by the ions. To estimate the uncertainty due to finite laser duration, we changed the interaction time between light and ions from 2 to 72 μs but maintained a constant measuring time of 76 μs. The relation between the photon counting and the interaction time is shown in Fig. 5. We can see that $N_{850,854}$ and N_{850} reach their maximum values during a time period of 2 μs or longer, but for N_{393} it needs about 30 μs to pump most of the ions to the D states. Because the lifetimes of the D states are finite, the ions in the D states may fall directly to the ground state and then be affected again by the 393-nm

TABLE I. Measurement uncertainties of the branching fraction for the $4P_{3/2} - 4S_{1/2}$ decay.

Effect	Shift	Error
Counting statistics	0	0.0004
Polarization alignment	0	0.00004
Loss of ions	$<1 \times 10^{-7}$	0
Finite laser durations	0.0004	0.0001
Finite lifetimes of D states	$< -3 \times 10^{-6}$	0
Extinction ratio of AOMs and off-resonant excitation	0.0002	0.0001
Unwanted components of lasers	0	$<5 \times 10^{-6}$
Total	0.0006	0.0004

TABLE II. Measurement uncertainties of the branching fraction for the $4P_{3/2} - 3D_{3/2}$ decay.

Effect	Shift	Error
Counting statistics	0	0.0001
Polarization alignment	0	4×10^{-6}
Loss of ions	$<1 \times 10^{-6}$	0
Finite laser durations	-4×10^{-5}	1×10^{-5}
Finite lifetimes of D states	$<3 \times 10^{-7}$	0
Extinction ratio of AOMs and off-resonant excitation	0.0002	0.0002
Unwanted components of lasers	0	$<1 \times 10^{-6}$
Total	0.0002	0.0002

laser; thus, the fluorescence counting may result in additional photons. The additional counting increases as time goes on, causing N_{393} to rise continuously after 30 μs. We estimated the error coming from finite laser durations as 0.0001 for the $4P_{3/2} - 4S_{1/2}$ decay and 1×10^{-5} for the $4P_{3/2} - 3D_{3/2}$ decay.

The finite lifetime of the D states can induce additional photons as we stated before. The infrared lights were turned on 40 μs later than the 393-nm laser pulse. Since the lifetime of D states is about 1.2 s, the ions have the probability of 3.3×10^{-5} to spontaneously decay into the ground state. This will cause a shift of less than -3×10^{-6} and 3×10^{-7} for p and q, respectively. Due to the extinction ratio, a light of small power can still go through the AOMs when the AOMs are turned off, which brings extra photon counts. Our AOMs extinction ratio is about 46 dB. To obtain a more accurate evaluation, we measured how many photons would be detected when AOMs are turned off. The photon counter does counting when the lasers are off, as shown in Fig. 3. The average of the photon counts will become stable as the counting time increases. At the same time, the collision of ions or other off-resonant excitations may also

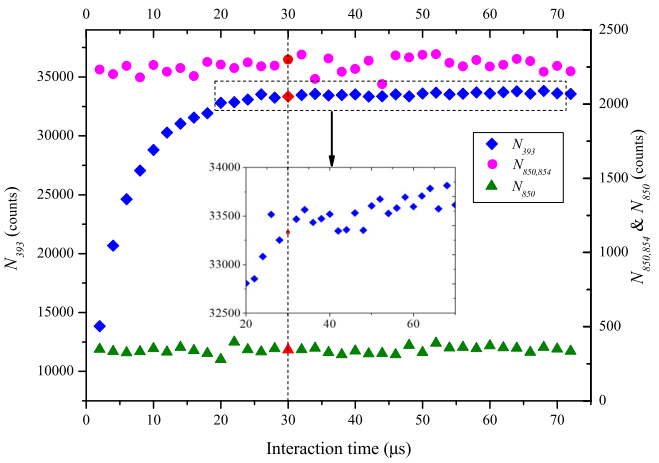

FIG. 5. Relation between photon counts and the interaction time between lasers and ions. The red dots mark the time duration of 30 μs used in our measurement. Each point is obtained by averaging four measured data.

cause extra photons. We estimated the errors due to the AOMs extinction ratio and off-resonant excitations to be 0.0001 and 0.0002 for the $4P_{3/2} - 4S_{1/2}$ and $4P_{3/2} - 3D_{3/2}$ decays, respectively, and the corresponding shifts to be 0.0002 and 0.0002.

The unperturbed branching fractions can be obtained when the angle between the light polarization and magnetic field is 54.7°. Since we measured two sets of data at two specific directions with an angle of 109.4°, it was not necessary to precisely determine the direction of magnetic field. The uncertainty evaluation was based on the measurement results shown in Fig. 4. According to the linear fitting, the slopes of the branching fractions p and q are about 0.001 and 0.01, respectively. The prism holder introduces a polarization uncertainty of 0.05°. In consideration of the uncertainty of laser direction, the error in angle is about 0.07°, causing the uncertainties of 4×10^{-5} and 4×10^{-6} for p and q, respectively.

The outputs of diode lasers include unwanted components, for example, the spectrum of the 393-nm diode laser includes a 397-nm background light, and the spectrum of the 850-nm diode laser includes a 854-nm background light. Two filters were inserted into the lasers' paths to filter out those unwanted components. The uncertainties due to unwanted components were estimated to be less than 5×10^{-6} and 1×10^{-6} for p and q, respectively.

In our experiment, ions will lose gradually. Photons at different times come from ions of different numbers. The difference between the detections of $N_{850,854}$ and N_{393} leads to an uncertainty in p. The density of ion crystals is constant under the constant radio frequency [43]. Larger crystals have higher ion losing speed. A volume change was detected within 10 minutes that could be used to determine the losing speed of ions. The ion losing speed is lower than 0.5 per 10 minutes when the crystal is as big as our ion trap can hold. The $N_{850,854}$ and N_{850} were detected at 6.3 and 12.6 ms after the N_{393} detection was made. Therefore, the ion loss has caused the shift of the branching fractions p and q to be 1×10^{-7} and 1×10^{-6}, respectively.

After averaging the measured values at −46.4° and 63° and taking into account of other uncertainty sources, the branching fractions were determined to be 0.9350(4) for the $4P_{3/2} - 4S_{1/2}$ decay, 0.0063(2) for the $4P_{3/2} - 3D_{3/2}$ decay, and 0.0587(4) for the $4P_{3/2} - 3D_{5/2}$ decay. Our results agree well with the experimental values reported by Gerritsma *et al.* [25] using a different method. If we combine the high-precision lifetime of the $4P_{3/2}$ state with the results determined in this work, we can extract the transition rates and the reduced matrix elements for the transitions from $4P_{3/2}$ to $4S_{1/2}$, $3D_{3/2}$, and $3D_{5/2}$. Although the lifetime of the $4P_{3/2}$ state has been measured by several groups [29–32], significant differences among these measured values remain. As mentioned in the Introduction, the branching fractions of the $4P_{1/2}$ state have been measured using two independent methods, and their measured values are in good accord. Therefore, these measured branching fractions for the $4P_{3/2}$ and $4P_{1/2}$ states can serve as a benchmark for testing relativistic atomic many-body methods. In the following section, we will present a calculation of the branching fractions for the $4P$ states using four approximate models, under the framework of relativistic coupled-cluster theory.

III. THEORETICAL RESULTS

The lifetime of a state $|\psi_v\rangle$ is defined by

$$\tau_v = \frac{1}{\sum_{o,w} A^o_{vw}}, \tag{6}$$

where A^o_{vw} is the transition rate due to a transition operator O, and the summation over o indicates that all allowed electromagnetic transitions from $|\psi_v\rangle$ should be included, such as electric dipole, electric quadrupole, magnetic dipole, and so on. The branching ratio for a certain transition channel is calculated by

$$R_{vw} = \frac{A_{vw}}{\sum_{o,i} A^o_{iw}}\,. \tag{7}$$

For the $4P$ states considered here, except the electric dipole transitions, contributions from other electromagnetic transitions are very small and they can thus be neglected. For the $4P_{3/2}$ state, there are three decay channels: $4P_{3/2} - 3D_{5/2}$, $4P_{3/2} - 3D_{3/2}$, and $4P_{3/2} - 4S_{1/2}$. For the $4P_{1/2}$ state, there are only two decay channels: $4P_{1/2} - 3D_{3/2}$ and $4P_{1/2} - 4S_{1/2}$.

The electric dipole transition rate A_{vw} can be expressed according to

$$A_{vw} = \frac{2.02616 \times 10^{18}}{\lambda^3 (2j_v + 1)} |\langle \Psi_v \| E1 \| \Psi_w \rangle|^2\,, \tag{8}$$

where λ represents the transition wavelength in Å and $\langle \Psi_v \| E1 \| \Psi_v \rangle$ is the reduced matrix element of the electric dipole operator. In this work, atomic wave functions and the transition matrix elements are calculated using the relativistic coupled cluster method (RCC).

In the framework of RCC, the wave function of an atom with a valence orbital v is generated by

$$|\Psi_v\rangle = e^S |\Phi_v\rangle\,, \tag{9}$$

where S is the cluster operator and $|\Phi_v\rangle$ is the reference state that is set to be the lowest-order Dirac-Fock wave function. The cluster operator S is expanded as a sum of n-particle excitations S_n of the lowest-order wave function

$$S = \sum_{n=1}^{N} S_n = S_1 + S_2 + S_3 + \cdots\,, \tag{10}$$

where N is the number of electrons of the system. In the linear single- and double-excitation approximation (LCCSD), the wave function is simplified as

$$|\Psi_v\rangle \approx (1 + S_1 + S_2)|\Phi_v\rangle\,. \tag{11}$$

If all nonlinear terms of single and double excitations (CCSD) are also considered, the wave function is then

$$\begin{aligned} |\Psi_v\rangle \approx \{1 + S_1 + S_2 + \tfrac{1}{2}\left(S_1^2 + S_2^2 + S_1 S_2\right) \\ + \tfrac{1}{6}\left(S_1^3 + 3S_1^2 S_2\right) + \tfrac{1}{24} S_1^4\}|\Phi_v\rangle\,. \end{aligned} \tag{12}$$

The excitations can be classified into two types: the core excitation and the excitation due to valence electrons, denoted by $S^{(0,0)}$ and $S^{(0,1)}$, respectively. Thus,

$$\begin{aligned} S &= S^{(0,0)} + S^{(0,1)} \\ &= S_1^{(0,0)} + S_2^{(0,0)} + S_1^{(0,1)} + S_2^{(0,1)}\,. \end{aligned} \tag{13}$$

TABLE III. Branching fractions for the $4P_{1/2}$ and $4P_{3/2}$ states of Ca^+. Uncertainties are given in parentheses.

Decay	Experiment		Theory					
	Present	Previous	LCCSD	$LCCSD_S$	CCSD	$CCSD_S$	Recommended	Previous
$4P_{3/2} \to 4S_{1/2}$	0.9350(4)	0.9347(3) [25]	0.93608	0.93443	0.93567	0.93547	0.9344(13)	0.9381 [9] 0.9354 [10] 0.9340 [11] 0.9350(62) [12]
$4P_{3/2} \to 3D_{5/2}$	0.0587(4)	0.0587(2) [25]	0.05746	0.05895	0.05783	0.05800	0.0590(12)	0.0556 [9] 0.0581 [10] 0.0593 [11] 0.0583(4) [12]
$4P_{3/2} \to 3D_{3/2}$	0.0063(2)	0.00661(4) [25]	0.00646	0.00662	0.00651	0.00653	0.0066(1)	0.00627 [9] 0.00649 [10] 0.00667 [11] 0.00666(4) [12]
$4P_{1/2} \to 4S_{1/2}$		0.93572(25) [26] 0.93565(7) [27]	0.93709	0.93545	0.93659	0.93641	0.9354(12)	0.9395 [9] 0.9366 [10] 0.9350 [11] 0.9374(74) [12]
$4P_{1/2} \to 3D_{3/2}$		0.06428(25) [26] 0.06435(7) [27]	0.06291	0.06455	0.06341	0.06359	0.0646(12)	0.0605 [9] 0.0634 [10] 0.0650 [11] 0.0626(5) [12]

In the language of second quantization, the cluster operator for the core excitation is

$$S^{(0,0)} = S_1^{(0,0)} + S_2^{(0,0)} = \sum_{ra} \{a_r^\dagger a_a\} s_a^r + \frac{1}{2} \sum_{rsab} \{a_r^\dagger a_s^\dagger a_a a_b\} s_{ab}^{rs}, \quad (14)$$

and the cluster operator for the valence excitation is

$$S^{(0,1)} = S_1^{(0,1)} + S_2^{(0,1)} = \sum_{r \neq v} \{a_r^\dagger a_v\} s_v^r + \sum_{rsa} \{a_r^\dagger a_s^\dagger a_v a_a\} s_{va}^{rs}. \quad (15)$$

In the above, a and b represent the core orbitals, r and s represent virtual orbitals, v denotes a valence state, $a^\dagger$ and a are, respectively, the single-particle creation and annihilation operators, and $s_{\cdots}^{\cdots}$ are the cluster amplitudes determined by solving the coupled equations that can be derived from the generalized Bloch equations by keeping only the connected terms [44].

After obtaining the cluster amplitudes, the transition matrix element of a one-particle operator Z between $|\Psi_v\rangle$ and $|\Psi_w\rangle$ can be evaluated according to

$$Z_{wv} = \frac{\langle \Psi_w | Z | \Psi_v \rangle}{\sqrt{\langle \Psi_w | \Psi_w \rangle \langle \Psi_v | \Psi_v \rangle}} = \frac{\langle \Phi_w | e^{S^\dagger} Z e^S | \Phi_v \rangle}{\sqrt{\langle \Phi_w | e^{S^\dagger} e^S | \Phi_w \rangle \langle \Phi_v | e^{S^\dagger} e^S | \Phi_v \rangle}}. \quad (16)$$

For calculating atomic properties, only the linearized terms of the coupled-cluster wave functions are included. Thus,

$$e^{S^\dagger} Z e^S \approx Z + \{S^{(0,0)\dagger} Z + \text{c.c.}\} + \{S^{(0,1)\dagger} Z + \text{c.c.}\} + S^{(0,0)\dagger} Z S^{(0,0)} + S^{(0,1)\dagger} Z S^{(0,1)} + \{S^{(0,0)\dagger} Z S^{(0,1)} + \text{c.c}\}, \quad (17)$$

and

$$e^{S^\dagger} e^S \approx 1 + S^{(0,0)\dagger} S^{(0,0)} + S^{(0,1)\dagger} S^{(0,1)}, \quad (18)$$

where c.c. represents the Hermitian conjugated part.

In the present work, we calculate the transition matrix elements using four approximate models: LCCSD, CCSD, $LCCSD_S$, and $CCSD_S$, where $LCCSD_S$ and $CCSD_S$ are the ones involving a semi-empirical scaling process. In the $LCCSD_S$ and $CCSD_S$ calculations, the single-excitation coefficients of the valence electron are replaced by new single-excitation coefficients that are equal to the old ones multiplied by the factor $\delta(E_v^{\text{Expt.}})/\delta(E_v^{\text{Theory}})$. $\delta(E_v)$ represents the correlation energy of the valence electron v, and $\delta(E_v^{\text{Expt.}}) = E_v^{\text{Expt.}} - E_v^{\text{DF}}$. In $LCCSD_S$, the scaling factors for $4S$, $4P$, and $3D$ states are, respectively, 0.9285, 0.9294, and 0.9210; and in $CCSD_S$, the corresponding factors are 0.9679, 0.9788, and 0.9858. The description of this semi-empirical scaling method can be found in Ref. [45]. The branching ratios of the $4P$ states of Ca^+ were calculated using our transition matrix elements, together with experimental transition energies from NIST [46]. In our calculations, 50 B-splines and the relativistic wave-function boundary conditions, proposed by Johnson *et al.* [47], were adopted to expand the large and small components of the radial wave function. All core orbitals were set to be active and the virtual orbitals whose energies smaller than 1500 atomic units and partial waves $\ell_{\max} \leqslant 6$ were included in the coupled-cluster calculation. More details about the relativistic coupled-cluster method based on B-spline basis can be found in Ref. [48].

In Table III, we list the branching fractions of the $4P_{1/2}$ and $4P_{3/2}$ states obtained by using LCCSD, $LCCSD_S$, CCSD, and $CCSD_S$ methods and compare to all available experimental [25–27] and theoretical results [9–12]. From Table III, we can see that the precision of these experimental results

are sufficient to differentiate among LCCSD, $LCCSD_S$, and CCSD models. The differences between CCSD and $CCSD_S$ results are very small, owing to the fact that the CCSD energies are very close to the experimental energies; in other words, the scaling factors of the CCSD model are close to 1. Among these models, the $LCCSD_S$ results are closest to the experimental values for both states of interest, but the LCCSD results are the worst ones. We also found that the biggest difference between the measured and LCCSDs results are smaller than the one between the $LCCSD_S$ and CCSD models. Therefore, we think that the $LCCSD_S$ results can be considered as the recommended values, and the difference between the $LCCSD_S$ and CCSD values are treated as the uncertainties. Our recommended results are consistent with the experimental values.

IV. SUMMARY

We demonstrated experimentally that the branching fractions for the $4P_{3/2}$ state of $^{40}Ca^+$ can be measured using the method of photon counting at the magic angle 54.7° between the magnetic field and laser polarization. Since it is very difficult to accurately determine the magic angle, we measured the branching fraction in two directions with an angle of 109.4°, and then calculated the average of the branching fractions in these two directions, based on the fact that the branching fractions are near-linearly dependent on the angle between the magnetic field and the laser polarization. In future, to acquire higher precision, we can increase photon counting time so that we can have more photons; we can also use double-pass AOMs to replace single-pass AOMs so that we can increase the extinction ratio. Our measured values of the branching fractions of the $4P_{3/2}$ state are consistent with the experimental values reported by Gerritsma *et al.* [25] using a different method. Once high-precision lifetime of the $4P_{3/2}$ state is available, we can combine our measured branching fractions with this lifetime and extract the transition rates and reduced matrix elements for the transitions from $4P_{3/2}$ to $4S_{1/2}$, $3D_{3/2}$, and $3D_{5/2}$. We also calculated the branching fractions for the $4P_{1/2}$ and $4P_{3/2}$ states using LCCSD, CCSD, $LCCSD_S$, and $CCSD_S$ approximations, and compared to the available experimental values. The comparisons showed that the theoretical results from $LCCSD_S$ are the closest to the experimental values for these two states. Our investigation in this work will be a valuable reference for studying other systems of similar structure, such as $Sr^+(n = 5)$, $Ba^+(n = 6)$, and $Ra^+(n = 7)$.

Note added. After submission of this work, we learned of the work by Meir *et al.* [49], which reports a value of the lifetime of the $4P_{3/2}$ state of $^{40}Ca^+$.

ACKNOWLEDGMENTS

We thank Cheng-Bin Li, Zong-Chao Yan, and Ting-Yun Shi for help and fruitful discussion. This work was supported by the National Key R&D Program of China (Grants No. 2017YFF0212003, No. 2017YFA0304401, No. 2017YFA0304404, and No. 2018YFA0307500), the Natural Science Foundation of China (Grants No. 11622434, No. 11504094, No. 11634013, No. 91736310, and No. 11804373), the Strategic Priority Research Program of the Chinese Academy of Sciences (Grant No. XDB21030100), China Postdoctoral Science Foundation (Grant No. 2017M622556), CAS Youth Innovation Promotion Association (Grants No. 2015274 and No. 2018364), and Hubei Province Science Fund for Distinguished Young Scholars (Grant No. 2017CFA040).

[1] M. Chwalla, J. Benhelm, K. Kim, G. Kirchmair, T. Monz, M. Riebe, P. Schindler, A. S. Villar, W. Hänsel, C. F. Roos, R. Blatt, M. Abgrall, G. Santarelli, G. D. Rovera, and P. Laurent, Phys. Rev. Lett. **102**, 023002 (2009).
[2] Y. Huang, H. Guan, P. Liu, W. Bian, L. Ma, K. Liang, T. Li, and K. Gao, Phys. Rev. Lett. **116**, 013001 (2016).
[3] J. Benhelm, G. Kirchmair, C. F. Roos, and R. Blatt, Nat. Phys. **4**, 463 (2008).
[4] G. Kirchmair, J. Benhelm, F. Zähringer, R. Gerritsma, C. F. Roos, and R. Blatt, Phys. Rev. A **79**, 020304(R) (2009).
[5] T. Pruttivarasin, M. Ramm, S. G. Porsev, I. I. Tupitsyn, M. S. Safronova, M. A. Hohensee, and H. Häffner, Nature (London) **517**, 592 (2015).
[6] B. K. Sahoo, Phys. Rev. A **99**, 050501(R) (2019).
[7] L. M. Hobbs, A. M. Lagrange-Henri, R. Ferlet, A. Vidal-Madjar, and D. E. Welty, Astrophys. J. **334**, L41 (1988).
[8] D. E. Welty, D. C. Morton, and L. M. Hobbs, Astrophys. J. **106**, 533 (1996).
[9] C. Guet and W. R. Johnson, Phys. Rev. A **44**, 1531 (1991).
[10] S.-S. Liaw, Phys. Rev. A **51**, R1723 (1995).
[11] B. Arora, M. S. Safronova, and C. W. Clark, Phys. Rev. A **76**, 064501 (2007).
[12] B. K. Sahoo, B. P. Das, and D. Mukherjee, Phys. Rev. A **79**, 052511 (2009).
[13] J. Mitroy and J. Y. Zhang, Eur. Phys. J. D **46**, 415 (2008).
[14] M. S. Safronova and U. I. Safronova, Phys. Rev. A **83**, 012503 (2011).
[15] Y.-B. Tang, H.-X. Qiao, T.-Y. Shi, and J. Mitroy, Phys. Rev. A **87**, 042517 (2013).
[16] J. Jiang, L. Jiang, X. Wang, D.-H. Zhang, L.-Y. Xie, and C.-Z. Dong, Phys. Rev. A **96**, 042503 (2017).
[17] L. Filippin, S. Schiffmann, J. Dohet-Eraly, D. Baye, and M. Godefroid, Phys. Rev. A **97**, 012506 (2018).
[18] P. Kumar, C.-B. Li, and B. K. Sahoo, J. Phys. B: At. Mol. Phys. **51**, 055101 (2018).
[19] S. Singh, M. Kaur, B. Arora, and B. K. Sahoo, Phys. Rev. A **98**, 013406 (2018).
[20] J. Jiang, L. Jiang, Z. W. Wu, D.-H. Zhang, L.-Y. Xie, and C.-Z. Dong, Phys. Rev. A **99**, 032510 (2019).
[21] P.-L. Liu, Y. Huang, W. Bian, H. Shao, H. Guan, Y.-B. Tang, C.-B. Li, J. Mitroy, and K.-L. Gao, Phys. Rev. Lett. **114**, 223001 (2015).
[22] F. Gebert, Y. Wan, F. Wolf, C. N. Angstmann, J. C. Berengut, and P. O. Schmidt, Phys. Rev. Lett. **115**, 053003 (2015).

[23] P. Zhang, J. Cao, H.-l. Shu, J. Yuan, J. Shang, K. Cui, S. Chao, S. Wang, D. Liu, and X. Huang, J. Phys. B: At. Mol. Phys. **50**, 015002 (2017).
[24] Y. Huang, H. Guan, M. Zeng, L. Tang, and K. Gao, Phys. Rev. A **99**, 011401(R) (2019).
[25] R. Gerritsma, G. Kirchmair, F. Zähringer, J. Benhelm, R. Blatt, and C. F. Roos, Eur. Phys. J. D **50**, 13 (2008).
[26] M. Ramm, T. Pruttivarasin, M. Kokish, I. Talukdar, and H. Häffner, Phys. Rev. Lett. **111**, 023004 (2013).
[27] M. Hettrich, T. Ruster, H. Kaufmann, C. F. Roos, C. T. Schmiegelow, F. Schmidt-Kaler, and U. G. Poschinger, Phys. Rev. Lett. **115**, 143003 (2015).
[28] H. Shao, Y. Huang, H. Guan, C. Li, T. Shi, and K. Gao, Phys. Rev. A **95**, 053415 (2017).
[29] A. Gallagher, Phys. Rev. **157**, 24 (1967).
[30] F. H. K. Rambow and L. D. Schearer, Phys. Rev. A **14**, 1735 (1976).
[31] R. N. Gosselin, E. H. Pinnington, and W. Ansbacher, Phys. Rev. A **38**, 4887 (1988).
[32] J. Jin and D. A. Church, Phys. Rev. Lett. **70**, 3213 (1993).
[33] H. Guan, H. Shao, Y. Qian, Y. Huang, P.-L. Liu, W. Bian, C.-B. Li, B. K. Sahoo, and K.-L. Gao, Phys. Rev. A **91**, 022511 (2015).
[34] H. Shao, Y. Huang, H. Guan, Y. Qian, and K. Gao, Phys. Rev. A **94**, 042507 (2016).
[35] H. Shao, Y. Huang, H. Guan, and K. Gao, J. Phys. B: At. Mol. Phys. **51**, 045002 (2018).
[36] D. De Munshi, T. Dutta, R. Rebhi, and M. Mukherjee, Phys. Rev. A **91**, 040501(R) (2015).
[37] J.-P. Likforman, V. Tugayé, S. Guibal, and L. Guidoni, Phys. Rev. A **93**, 052507 (2016).
[38] H. Zhang, M. Gutierrez, G. Hao Low, R. Rines, J. Stuart, T. Wu, and I. Chuang, New J. Phys. **18**, 123021 (2016).
[39] M. Fan, C. A. Holliman, A. L. Wang, and A. M. Jayich, Phys. Rev. Lett. **122**, 223001 (2019).
[40] U. Fano and J. H. Macek, Rev. Mod. Phys. **45**, 553 (1973).
[41] L.-J. Du, T. Chen, H.-F. Song, S.-L. Chen, H.-X. Li, Y. Huang, X. Tong, K.-L. Gao, and H. Guan, Chin. Phys. B **24**, 083702 (2015).
[42] W. Qu, Y. Huang, H. Guan, X. Huang, and K. Gao, Chin. J. Lasers **38**, 0802008 (2011).
[43] L.-J. Du, H.-F. Song, H.-X. Li, S.-L. Chen, T. Chen, H.-Y. Sun, Y. Huang, X. Tong, H. Guan, and K.-L. Gao, Chin. Phys. B **24**, 113703 (2015).
[44] I. Lindgren and J. Morrison, *Atomic Many-Body Theory*, 2nd ed., (Springer, New York, 1987), Vol. 26, p. 1362 .
[45] M. S. Safronova and U. I. Safronova, Phys. Rev. A **83**, 052508 (2011).
[46] A. Kramida, Y. Ralchenko, J. Reader, and NIST ASD Team, "NIST Atomic Spectra Database (version 5.4.0)" (2016).
[47] W. R. Johnson, S. A. Blundell, and J. Sapirstein, Phys. Rev. A **37**, 307 (1988).
[48] Y.-B. Tang, B.-Q. Lou, and T.-Y. Shi, Phys. Rev. A **96**, 022513 (2017).
[49] Z. Meir, M. Sinhal, M. S. Safronova, and S. Willitsch, arXiv:1909.10516.